Journal of Zhejiang University-SCIENCE A (Applied Physics & Engineering) 2025 26(8):755-770
www.jzus.zju.edu.cn; www.springer.com/journal/11582
E-mail: jzus_a@zju.edu.cn

Research Article

https://doi.org/10.1631/jzus.A2500150

Continuous energy exchange between magnetic fields supporting memristive neuron firing

Zhao LEI[1], Qun GUO[1], Chunni WANG[2], Jun MA[1,2]✉

[1]*School of Automation and Electrical Engineering, Lanzhou University of Technology, Lanzhou 730050, China*
[2]*Department of Physics, Lanzhou University of Technology, Lanzhou 730050, China*

Abstract: Biological neurons can be excited to maintain certain firing patterns following different external stimuli, and similar changes in electrical activities can be reproduced in some neural circuits by applying an external voltage. Generic neural circuits are composed of capacitors, induction coils, resistors, and nonlinear resistors, and continuous energy exchange between the capacitive and inductive components is crucial for preserving output voltages. Incorporating nonlinear elements causes interactions between the charge flow across the capacitor and the induced electromotive force on the inductor. It is a challenge to explore the occurrence of nonlinear oscillation and coherence resonance in a neural circuit without using a capacitor and nonlinear resistor, and it considers the case lack of electric field energy. In this paper, a simple neural circuit is proposed that combines two inductors, one magnetic flux-controlled memristor (MFCM), and three resistors, with two constant voltage sources in the branch circuits used as reverse potentials in the ion channels. The field energy has an exact form, and it is stored in the circuit components as a magnetic field. Scale transformation is applied on the circuit equations and field energy function to obtain equivalent dimensionless forms of the memristive neuron and Hamilton energy. The reference values for the physical time and capacitance are represented by an appropriate combination of resistance and inductance, because the capacitance value is unavailable. The memristive neuron without capacitive effect still shows similar firing patterns, and coherence resonance is induced under noisy excitation. The emergence of coherence resonance can be predicted by calculating the distribution of the average energy $\langle H \rangle$ versus noise intensity, and the value for $\langle H \rangle$ reaches a maximum under coherence resonance. Finally, an adaptive law for parameter growth under energy control is proposed to control mode transitions in the electrical activity. The methodology and results of this work offer insights into the oscillatory mechanism of neural circuits, and showcase how magnetic field control can be used to manage neural activations.

Key words: Neural circuit; Hamilton energy; Memristor; Stochastic resonance; Adaptive parameter growth

1 Introduction

Changes in membrane potentials result in cascading electrical activities, with neurons maintaining suitable energy levels. These processes, which are facilitated by membrane ion channels, voltage-gate regulation, and local feedback loops, constitute neural circuits that serve as the fundamental units of neural information processing (Sporns, 2010). These circuits exhibit diverse firing patterns, such as spiking, bursting, and rhythmic firings; such firings can match with membrane responses, action potential timings, and postsynaptic integration effects (Isaac et al., 1997; Douglas and Martin, 2004). Research has shown that neuronal firing is regulated not only by external stimuli, but also by the intrinsic energy level of a neuron and local synaptic inputs, especially inhibitory signals (Buzsáki and Draguhn, 2004; Izhikevich, 2006; Wang, 2010). For instance, Froemke et al. (2007) found that inhibitory neurons can modulate the threshold for long-term potentiation (LTP) induction in excitatory neurons within specific circuits, thereby shaping the plasticity window. Moreover, Katz and Shatz (1996) observed that spontaneous neuronal firing can form stable synaptic connectivity patterns, influencing a neuron's role within functional small-scale networks.

✉ Jun MA, hyperchaos@lut.edu.cn
Zhao LEI, https://orcid.org/0000-0002-8046-0650
Chunni WANG, https://orcid.org/0000-0002-4688-7888
Jun MA, https://orcid.org/0000-0002-6127-000X

Received Apr. 25, 2025; Revision accepted June 2, 2025;
Crosschecked July 21, 2025; Online first Aug. 8, 2025

When neurons aggregate into localized functional regions, electromagnetic field coupling among cells can influence action potential propagation and synaptic plasticity, due to regulation of energy and controllable modification of ion channels (Takembo et al., 2019; Wang et al., 2019). Takembo et al. (2019) demonstrated that electromagnetic radiation alters the spatiotemporal patterns of membrane potentials within neural networks, affecting both synaptic coupling and plasticity. Wang et al. (2019) showed that electromagnetic induction and radiation via field coupling can modulate inter-neuronal communication, and that signal processing in a neural network can be activated under field coupling even when synaptic connections are removed. Neural networks maintain functional stability by regulating synaptic strength in order to balance excitation and inhibition; this balance is essential for their normal operation (Brütt and Kaernbach, 2021; Chen et al., 2022; Kirischuk, 2022). Disruption of this balance may lead to pathological conditions such as epilepsy (Gao et al., 2017). Electromagnetic fields can regulate this balance by altering synaptic strengths, selectively enhancing or weakening specific connections in a parameter tuning approach (Dagar et al., 2016). Therefore, reconstructing neural circuits from the single-cell level not only reveals the fundamental principles of neural information encoding, but also provides cell-level intervention targets that aid understanding and treatment of neurological disorders (Altan et al., 2024).

In traditional circuit theory, the dynamic exchange of energy is typically attributed to the interaction between electric field components (e.g., capacitors) and magnetic field components (e.g., inductors) (Cheng et al., 2007; Li et al., 2016; Moon and Leeb, 2016; Schroedermeier and Ludois, 2017). Capacitors serve as key energy storage elements, and provide the physical foundation for behaviors in oscillatory circuits such as periodic oscillation, signal modulation, and neuron-like firings (Indiveri et al., 2011). Consequently, most circuit designs rely heavily on capacitors to emulate the capacitive properties of neuron cell membranes (Jia JN et al., 2023, 2024; Wan et al., 2024; Wang et al., 2024; Yang et al., 2024a, 2024b). However, the relatively large physical dimensions and challenges of integrating capacitors hinder their application in high-density, flexible, and nanoscale neural networks. Thus, developing novel components and architectures without connecting capacitors, which can replicate neural circuit functionality and save electric field energy, has become a critical focus in neuroelectronic engineering. However, lacking capacitors in a neural circuit presents new difficulties for scale transformation when the circuit equations are mapped to dimensionless theoretical models. This is because a reference capacitance is crucial for setting the reference time and energy. Therefore, an effective combination of electric components is crucial for realizing such scale transformations, and then nonlinear analysis can be calculated in the dimensionless models through a numerical approach.

Chua ever defined the concept of memristor in 1971, filling the role of the fourth basic circuit element after resistors, capacitors, and inductors. A memristor exhibits unique properties such as nonlinear modulation, memory retention, and dynamic energy responsiveness (Chua, 1971; Strukov et al., 2008; Pershin and di Ventra, 2011). Based on their operational principles, memristors can be categorized into magnetic field-controlled memristors (MFCMs) and charge-controlled memristors (CCMs). MFCMs employ magnetic flux variation as the control variable, highlighting a bidirectional regulatory relationship between magnetic field flux and the memristive states (Li et al., 2021; Xu et al., 2024a). In contrast, CCMs are governed primarily by charge or voltage changes, offering faster response times and more mature device architectures. CCMs have been widely employed in large-scale memory arrays, artificial synaptic circuits, and low-power logic devices (Chen et al., 2015; Xu et al., 2024b; Lei and Ma, 2025). Despite differences in their underlying mechanisms, both types of memristors play essential roles in the construction of neuromorphic circuits and the functional enhancement of neural circuits.

The introduction of an MFCM into the branch circuit of a neural circuit supports energy shunting in the form of magnetic flux. An MFCM-coupled neural circuit can estimate and describe the effect of a magnetic field, and its equivalent dimensionless model (a memristive neuron) often stores the magnetic flux variable; here, the memristive term is considered as an induction current for electromagnetic induction. Through combinations with a variety of sensing elements (such as thermistors, photocells, piezoelectric ceramics, and Josephson junctions), various functional

neural circuits can be constructed. Such functional neurons can be sensitive to different external stimuli, such as temperature, light, mechanical vibrations, and magnetic fields (Ma et al., 2019; Ma, 2023).

In this study, two inductors connected in parallel are used to couple an MFCM, and external stimuli and noise radiation are applied to detect characteristic features of neural activity. An exact energy function for the neuron model is defined, and it is further proved according to fundamental physical laws, including the Helmholtz theorem. The average energy is analyzed statistically, and used to predict the stochastic resonance (SR), a phenomenon which is also observed in some mathematical and biological neuron models. In particular, during scale transformation from the circuit equations to the equivalent dimensionless neuron modes, $[L/R]$ (=$[T]$) and $[L/R^2]$ (=$[C]$) are employed as reference values to replace the time reference and capacitance reference, respectively. This scale transformation is effective for mapping the neural circuit to an effective neuron model, even though a capacitive variable is not used. Our methodology offers new theoretical insights and practical guidance for designing effective and robust neural circuits.

2 Model and scheme

The magnetic field components in this system primarily consist of inductors and an MFCM, which collectively serve as storage media for magnetic field energy. A major goal of this study is to verify whether this magnetic field-dependent circuit can generate spontaneous oscillations without utilizing capacitive field energy. When nonlinear activation and regulation from the MFCM are activated, the neural circuit in this work gains the capability to exhibit firing activities by pumping magnetic field among different ion channels/branch circuits of the neural circuit. In constructing equivalent oscillator-type theoretical models, the conversion of physical variables into dimensionless parameters using reference time and reference voltage is a critical modeling step. As illustrated in Fig. 1, we designed a minimalistic neural circuit architecture comprised of two inductors, one MFCM, and three resistors, which deliberately excludes conventional capacitive elements and nonlinear resistive components.

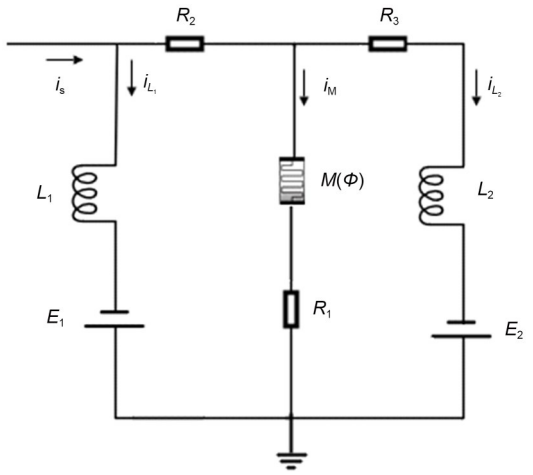

Fig. 1 Proposed MFCM coupled neural circuit driven by forcing current i_s. R_1, R_2, R_3, L_1, L_2, E_1, and E_2 denote three resistors, two inductors, and two constant voltage sources, respectively. $M(\phi)$ marks the mem-conductance of the MFCM, and ϕ is the magnetic flux passing through the memristor (M)

Observing Fig. 1, the constant voltages E_1 and E_2 constrain the channel currents (i_M, i_{L_1}, and i_{L_2}), and each can be considered as a reverse potential of ion channels in biological neurons. The linear resistors R_1, R_2, and R_3 balance the channel voltage through the consumption of Joule heat. The branch circuit composed of the MFCM measures the membrane potential, and energy flow is shunted between the parallel branch circuits. The MFCM can be described by:

$$\begin{cases} i_M = M(\phi)V_M = \beta \csc(\phi)V_M, \\ i_M = i_s - i_{L_1} - i_{L_2}, \\ \dfrac{\mathrm{d}\phi}{\mathrm{d}t} = -K\phi + \delta V_M. \end{cases} \tag{1}$$

In Eq. (1), V_M is the voltage across the terminals of the MFCM with mem-conductance $M(\phi)$, the parameter β accounts for the material properties of the MFCM, and the parameters (K, δ) estimate the effect of the magnetic field on the memristive channel/branch circuit. Indeed, the parameter $\delta=1/N_0$ when the MFCM is considered as an equivalent induction coil with N_0 turns; the parameter K estimates the effect of present magnetic field on the changes of magnetic flux, and it holds a physical unit as frequency. The field energy in the three components is estimated as follows:

$$\begin{cases} W_{L_1}=\dfrac{1}{2}L_1 i_{L_1}^2, \\ W_{L_2}=\dfrac{1}{2}L_2 i_{L_2}^2, \\ W_{\mathrm{M}}=\dfrac{1}{2}\phi i_{\mathrm{M}}, \\ W=\dfrac{1}{2}L_1 i_{L_1}^2+\dfrac{1}{2}L_2 i_{L_2}^2+\dfrac{1}{2}\phi i_{\mathrm{M}}. \end{cases} \tag{2}$$

Equivalent conversion from physical variables to dimensionless variables is crucial for developing theoretical models from neural circuits. This is because the numerical solution approach should be independent of the physical units. The reference time [T], reference voltage [V_0], and reference capacitance [C] are important for the selection of reference values, and the symbol [*] signifies an operation on physical units. One of the constant voltages (E_1, E_2) can be used as a reference voltage V_0 for scale transformation on the physical variables, considering the elements in Fig. 1. Because of the absence of capacitor in the circuit in Fig. 1, an equivalent combination of other physical parameters is used to define equivalent reference values as follows (Guo and Ma, 2025):

$$[T]=\left[\frac{Q}{I}\right]=\left[\frac{CV}{I}\right]=[RC]=\left[\frac{\Phi}{V}\right]=\left[\frac{LI}{IR}\right]=\left[\frac{L}{R}\right],$$
$$[C]=\left[\frac{L}{R^2}\right], \tag{3}$$

where the operation [*] removes physical units from physical variables including voltage, current, charge, and time; T, R, C, L, Q, Φ, and I indicate physical time, resistance, capacitance, inductance, charge, magnetic flux, and current intensity, respectively. The physical variables in Fig. 1 become coherent in following the circuit equations:

$$\begin{cases} L_1\dfrac{\mathrm{d}i_{L_1}}{\mathrm{d}t}=(i_{\mathrm{s}}-i_{L_1})R_2+V_{\mathrm{M}}+i_{\mathrm{M}}R_1+E_1, \\ L_2\dfrac{\mathrm{d}i_{L_2}}{\mathrm{d}t}=V_{\mathrm{M}}+i_{\mathrm{M}}R_1+E_2-i_{L_2}R_3, \\ \dfrac{\mathrm{d}\phi}{\mathrm{d}t}=-K\phi+\delta V_{\mathrm{M}}. \end{cases} \tag{4}$$

There are three branch circuits in the neural circuit presented in Fig. 1, and no capacitive components are used. Neurons/cells have small geometric dimensions, and their capacitance values can be ignored when stochastic diffusion and intracellular ion pumping induce distinct magnetic fields. On the other hand, the damage in capacitor or missing in capacitor requires new schemes for maintaining the electrical signals from the neural circuit. Therefore, two inductors and one MFCM are used in the three-branch circuits for describing the effect of the magnetic field and electromagnetic induction, respectively. When an external electric stimulus i_{s} is applied, energy is shunted between the three branches of the circuit, and then the memristive channel is controlled to offer different memristive potentials accompanied by suitable energy levels. Following the definition for reference time in Eq. (3), some new variables and dimensionless gains are defined through:

$$\begin{cases} x=\dfrac{R_1 i_{L_1}}{E_1},\ y=\dfrac{R_1 i_{L_2}}{E_1},\ z=\dfrac{R_1\phi}{L_1E_1},\ \tau=\dfrac{tR_1}{L_1}, \\ i_{\mathrm{s}}'=\dfrac{i_{\mathrm{s}}R_1}{E_1},\ a=\dfrac{E_2}{E_1},\ b=\dfrac{R_3}{R_1},\ c=\dfrac{L_1}{L_2}, \\ r=\dfrac{R_2}{R_1},\ k=K\dfrac{L_1}{R_1},\ \sigma=\dfrac{L_1E_1}{R_1},\ \beta'=\dfrac{1}{\beta R_1}, \end{cases} \tag{5}$$

where t represents the physical time and τ is a dimensionless time. Inserting the new variables and parameters above into Eq. (4), and then a memristive oscillator is obtained by:

$$\begin{cases} \dfrac{\mathrm{d}x}{\mathrm{d}\tau}=ri_{\mathrm{s}}'-rx+(i_{\mathrm{s}}'-x-y)(\beta'\sin(\sigma z)+1)+1, \\ \dfrac{\mathrm{d}y}{\mathrm{d}\tau}=c[(i_{\mathrm{s}}'-x-y)(\beta'\sin(\sigma z)+1)-by+a], \\ \dfrac{\mathrm{d}z}{\mathrm{d}\tau}=-kz+\delta(i_{\mathrm{s}}'-x-y)\beta'\sin(\sigma z). \end{cases} \tag{6}$$

The external stimulus i_{s}' can be adjusted to modify the oscillatory state in the memristive neuron, even when all parameters are fixed. The voltage variable V_{M} can also be set to discern the firing modes as follows:

$$\begin{cases} V_{\mathrm{M}}=\dfrac{i_{\mathrm{s}}-i_{L_1}-i_{L_2}}{\beta\csc(\phi)}, \\ u=\dfrac{V_{\mathrm{M}}}{E_1}=(i_{\mathrm{s}}'-x-y)\beta'\sin(\sigma z), \end{cases} \tag{7}$$

where u is the memristive potential.

As presented in Eq. (1), the mem-conductance has a csc(*) form, despite most previous research opting

for a cubic or hyperbolic form. In fact, setting csc(*) mem-conductance or sin(*) mem-resistance for the memristor accounts for the polarization and depolarization of excitable media in a periodic fashion, because continuous electric excitations affect the neuron and excitable media. From a dynamic viewpoint, the memristor can be configured with different definitions for the relation between charge and magnetic flux, and then the memristive term with high-order nonlinearity can support continuous oscillation in the electrical activities. However, missing the capacitive variable as derived from a capacitor in the neural circuit prevents extensive energy exchange between the magnetic field and electric field. Therefore, carefully setting the memristive term for the neural circuit and its equivalent theoretical model requires periodic excitation to induce continuous electrical activities, and thus the csc(*) memristive term is useful. Consequently, the field energy in Eq. (2) is updated to a dimensionless form as follows:

$$\begin{cases} H_{L_1}=\dfrac{1}{2}x^2, \\ H_{L_2}=\dfrac{1}{2c}y^2, \\ H_{\mathrm{M}}=\dfrac{1}{2}z(i_{\mathrm{s}}'-x-y), \\ H=\dfrac{R_1^2W}{L_1E_1^2}=\dfrac{1}{2}x^2+\dfrac{1}{2c}y^2+\dfrac{1}{2}z(i_{\mathrm{s}}'-x-y). \end{cases} \tag{8}$$

That is, the Hamilton energy H converted from the field energy W has three terms, which are associated with the magnetic field in two inductors and the MFCM, respectively. Eq. (6) is rewritten in an equivalent vectorized form to approach its sole energy function following the Helmholtz theorem, in which the electromagnetic field is considered as a superposition of vortex field and gradient field:

$$\begin{pmatrix} \dfrac{\mathrm{d}x}{\mathrm{d}\tau} \\ \dfrac{\mathrm{d}y}{\mathrm{d}\tau} \\ \dfrac{\mathrm{d}z}{\mathrm{d}\tau} \end{pmatrix} = \begin{bmatrix} ri_{\mathrm{s}}'-rx+(i_{\mathrm{s}}'-x-y)(\beta'\sin(\sigma z)+1)+1 \\ c[(i_{\mathrm{s}}'-x-y)(\beta'\sin(\sigma z)+1)-by+a] \\ -kz+\delta(i_{\mathrm{s}}'-x-y)\beta'\sin(\sigma z) \end{bmatrix} =$$

$$\boldsymbol{F}_{\mathrm{c}}(x,\,y,\,z)+\boldsymbol{F}_{\mathrm{d}}(x,\,y,\,z)=$$

$$\nabla H^{\mathrm{T}}\boldsymbol{J}(x,\,y,\,z)\nabla H+\nabla H^{\mathrm{T}}\boldsymbol{R}(x,\,y,\,z)\nabla H=$$

$$\begin{bmatrix} F_{\mathrm{cx}} \\ F_{\mathrm{cy}} \\ F_{\mathrm{cz}} \end{bmatrix}+\begin{bmatrix} F_{\mathrm{dx}} \\ F_{\mathrm{dy}} \\ F_{\mathrm{dz}} \end{bmatrix}=\begin{bmatrix} 0 & 0 & C_1 \\ 0 & 0 & C_2 \\ -C_1 & -C_2 & 0 \end{bmatrix}\cdot \begin{bmatrix} x-0.5z \\ \dfrac{y}{c}-0.5z \\ 0.5(i_{\mathrm{s}}'-x-y) \end{bmatrix}+\begin{bmatrix} A_1 & 0 & 0 \\ 0 & A_2 & 0 \\ 0 & 0 & A_3 \end{bmatrix}\begin{bmatrix} x-0.5z \\ \dfrac{y}{c}-0.5z \\ 0.5(i_{\mathrm{s}}'-x-y) \end{bmatrix}, \tag{9a}$$

$$\begin{aligned} &C_1=2+2\beta'\sin(\sigma z), \\ &C_2=2c+2c\beta'\sin(\sigma z), \\ &F_{\mathrm{cx}}=(i'-x-y)(\beta'\sin(\sigma z)+1), \\ &F_{\mathrm{cy}}=c[(i'-x-y)(\beta'\sin(\sigma z)+1)], \\ &F_{\mathrm{cz}}=(-2x-2y+cz+z)(\beta'\sin(\sigma z)+1), \\ &F_{\mathrm{dx}}=ri_{\mathrm{s}}'-rx+1,\ \ F_{\mathrm{dy}}=c(-by+a), \\ &F_{\mathrm{dz}}=-kz+\delta(i_{\mathrm{s}}'-x-y)\beta'\sin(\sigma z)- \\ &\qquad(-2x-2y+cz+z)(\beta'\sin(\sigma z)+1), \\ &A_1=\frac{ri_{\mathrm{s}}'-rx+1}{x-0.5z},\ \ A_2=\frac{c(-by+a)}{\dfrac{y}{c}-0.5z}, \\ &A_3=\frac{F_{\mathrm{dz}}}{0.5(i_{\mathrm{s}}'-x-y)}. \end{aligned} \tag{9b}$$

Here, $\boldsymbol{F}_{\mathrm{c}}(x, y, z)$ and $\boldsymbol{F}_{\mathrm{d}}(x, y, z)$ represent the vortex field and gradient field, respectively. $\boldsymbol{J}(x, y, z)$ is a skew-symmetric matrix, while $\boldsymbol{R}(x, y, z)$ is a main diagonal matrix with elements including A_1, A_2, and A_3. It is important to clarify why the decomposition in Eq. (9) still has physical significance, even though the field energy in Eq. (2) is only endowed with the magnetic field form. In fact, two constant voltage sources are used in the circuit in Fig. 1, and they account for the resting potentials of the ion channels; however, they also provide electric field energy. Therefore, decomposition of the theoretical model into vector form is meaningless when the neural circuit has no electric field component, and the dimensionless energy must be obtained by directly applying the scale transformation to the physical field energy. Based on Helmholtz's theorem, the Hamilton energy function H for Eq. (8) meets the following criterion:

$$\begin{cases} \nabla H^{\mathrm{T}}\boldsymbol{F}_{\mathrm{c}}(x,\,y,\,z)=0, \\ \nabla H^{\mathrm{T}}\boldsymbol{F}_{\mathrm{d}}(x,\,y,\,z)=\dot{H}=\dfrac{\mathrm{d}H}{\mathrm{d}\tau}. \end{cases} \tag{10}$$

Indeed, the energy function H in Eq. (8) satisfies the solution of Eq. (10) according to Eq. (9), and we simplify and validate this as follows:

$$\begin{aligned}
&\nabla H^{\mathrm{T}}\boldsymbol{F}_{\mathrm{c}}=F_{\mathrm{cx}}\frac{\partial H}{\partial x}+F_{\mathrm{cy}}\frac{\partial H}{\partial y}+F_{\mathrm{cz}}\frac{\partial H}{\partial z}=0,\\
&\frac{\mathrm{d}H}{\mathrm{d}\tau}=\left(x-\frac{1}{2}z\right)\frac{\mathrm{d}y}{\mathrm{d}\tau}+\left(\frac{y}{c}-\frac{1}{2}z\right)\frac{\mathrm{d}y}{\mathrm{d}\tau}+\\
&\qquad\frac{1}{2}(i_{\mathrm{s}}'-x-y)\frac{\mathrm{d}z}{\mathrm{d}\tau}=\left(x-\frac{1}{2}z\right)F_{\mathrm{dx}}+\\
&\qquad\left(y-\frac{1}{2}cz\right)F_{\mathrm{dy}}+\frac{1}{2}(i_{\mathrm{s}}'-x-y)F_{\mathrm{dz}},\\
&\nabla H^{\mathrm{T}}\boldsymbol{F}_{\mathrm{d}}=F_{\mathrm{dx}}\frac{\partial H}{\partial x}+F_{\mathrm{dy}}\frac{\partial H}{\partial y}+F_{\mathrm{dz}}\frac{\partial H}{\partial z}=\frac{\mathrm{d}H}{\mathrm{d}\tau}.
\end{aligned}\tag{11}$$

In fact, an exact solution of Eq. (10) is the same Hamilton energy function as presented in Eq. (8). Therefore, the Hamilton energy function for the memristive neuron can be obtained by applying the scale transformation to the electric field energy components, and it can be proved by applying the Helmholtz theorem. When the energy function is available, the average energy <H> provides a feasible way to predict the stochastic resonance and coherence resonance in the neuron under noisy excitation. For simplicity, Gaussian white noise with zero average value and intensity D can be used to excite the neuron from different branch circuits or ion channels. <H> represents the mean value of the energy function in Eq. (8) within a transient period, as the running time in the numerical approach.

Most biological neurons remain in a quiescent state until a powerful-enough external stimulus is applied to trigger firing patterns, because they are not self-oscillatory. In the absence of external stimuli, the neuron model has finite equilibrium points, while external periodic forcing will generate increasingly more, approaching infinite, equilibrium points. The appearance of unstable equilibrium points is crucial for inducing chaos in the oscillatory states and continuous firing patterns. According to Eq. (6), and following the constraints $\mathrm{d}x/\mathrm{d}\tau=\mathrm{d}y/\mathrm{d}\tau=\mathrm{d}z/\mathrm{d}\tau=0$, the equilibrium points can be found according to the solution's dependence on the external excitation i_{s}'. At $i_{\mathrm{s}}'=0$, finite equilibrium points are obtained by solution with the following constraints:

$$\begin{cases}
0=-rx-(x+y)(\beta'\sin(\sigma z)+1)+1,\\
0=-(x+y)(\beta'\sin(\sigma z)+1)-by+a,\\
0=-kz-\delta(x+y)\beta'\sin(\sigma z).
\end{cases}\tag{12}$$

On the other hand, $i_{\mathrm{s}}'\neq 0$ enables infinite equilibrium points because it acts as a similar term to the jerk function $\sin(\sigma z)$ in Eq. (6), and thus chaos and multiple firing patterns in the electrical activities occur. Assuming any constant value for i_{s}', the corresponding Jacobi matrix and the dispersion relation are expressed by:

$$\boldsymbol{J}=\begin{bmatrix}f_1 & f_2 & f_3\\ g_1 & g_2 & g_3\\ h_1 & h_2 & h_3\end{bmatrix}.\tag{13}$$

The matrix elements and terms of Eq. (13) are given in Eq. (14), and a numerical solution can be obtained when all parameters are fixed:

$$\begin{cases}
f_1=-r-\beta'\sin(\sigma z)-1,\\
f_2=-\beta'\sin(\sigma z)-1,\\
f_3=i_{\mathrm{s}}'\beta'\sigma\cos(\sigma z)-\beta'\sigma(x+y)\cos(\sigma z),\\
g_1=c[-\beta'\sin(\sigma z)-1],\\
g_2=c[-\beta'\sin(\sigma z)-1-b],\\
g_3=c[i_{\mathrm{s}}'\beta'\sigma\cos(\sigma z)-\beta'\sigma(x+y)\cos(\sigma z)],\\
h_1=-\delta\beta'\sin(\sigma z),\\
h_2=-\delta\beta'\sin(\sigma z),\\
h_3=-k+\delta\beta'\sigma(i_{\mathrm{s}}'-x-y)\cos(\sigma z),
\end{cases}\tag{14}$$

$$\begin{aligned}
P(\lambda)=0=&(\lambda-f_1)(\lambda-g_2)(\lambda-h_3)-\\
&f_2g_3h_1-f_3g_1h_2-(\lambda-g_2)f_3h_1-\\
&(\lambda-f_1)h_2g_3-(\lambda-h_3)f_2g_1.
\end{aligned}\tag{15}$$

Here, λ represents the characteristic value of the system, and $P(\lambda)$ represents the characteristic value function. The system's numerical solutions become detectable when all parameters remain fixed. To examine noise effects, additive Gaussian white noise is independently introduced to affect each variable in Eq. (6), with each variable corresponding to an individual branch circuit in Fig. 1. Setting the parameters a=0.1, b=7.2, c=0.05, δ=1.5, β'=3.2, k=0.1, r=0.1, σ=20, and i_{s}'=5.0, 15 eigenvalues are obtained and listed in Table 1.

By systematically adjusting the noise intensity, we can observe its dynamic influence on both the shift in energy levels and the electrical activity patterns. This modulation approach enables effective detection of subtle system state changes. Our investigation

Table 1 Solutions and eigenvalues in Eq. (6)

No.	Equilibrium point	λ_1	λ_2	λ_3
1	(5.944083652, −0.1118877271, −1.100935654)	79.66907219	−0.3438747826	−1.167342297
2	(6.075855048, −0.1100575688, 1.100744755)	92.66929547	−0.3438725449	−1.165224189
3	(6.066321320, −0.1101899817, 0.9414520500)	−0.3438743352	−1.166933581	−91.79956077
4	(5.953637127, −0.1117550399, −0.9413129975)	−0.3438724191	−1.165085770	−80.97805975
5	(6.038210594, −0.1105804084, 0.4717686726)	88.98267979	−0.3438730558	−1.165707400
6	(5.981737442, −0.1113647577, −0.4718035671)	83.41298105	−0.3438740018	−1.166602622
7	(6.019387128, −0.1108418454, 0.1572599350)	87.13175055	−0.3438733448	−1.165980873
8	(6.000562765, −0.1111032949, −0.1572638084)	85.27530538	−0.3438736594	−1.166278452
9	(6.057033217, −0.1103189831, 0.7862633296)	90.82842603	−0.3438727898	−1.165455828
10	(5.962911096, −0.1116262348, −0.7863604453)	81.54438138	−0.3438743751	−1.166956181
11	(6.047538405, −0.1104508555, 0.6276208446)	−0.3438740793	−1.166686571	−90.00420332
12	(5.972415410, −0.1114942304, −0.6275591899)	−0.3438728107	−1.165463072	−82.79059229
13	(6.028756301, −0.1107117180, 0.3138032030)	−0.3438738013	−1.166418244	−88.20582606
14	(5.991194744, −0.1112334063, −0.3137878112)	−0.3438731696	−1.165808991	−84.59923658
15	(6.009975062, −0.1109725686, 0)	−0.3438734988	−1.166126501	−86.40423937

reveals that when external energy is injected into the memristive channel, it is redistributed to the two parallel inductive channels. This unique energy reallocation mechanism not only sustains continuous oscillations in the neural circuit, but also ensures stable electrical activities in the memristive neuron.

3 Numerical results and discussion

The time series values of the three variables in Eq. (6) and the memristive potential u in Eq. (7) are calculated by using the fourth-order Runge-Kutta algorithm. The external stimulus is selected as a sinusoidal excitation $i_s'=A\sin(\omega\tau)$, where A is the amplitude and ω is the angular frequency. In Fig. 2, we conducted an equilibrium point analysis and dynamical characterization by measuring the peak values, and the largest Lyapunov exponent (LLE) is estimated from the sampled time series for one variable.

The parameter σ governs the transition pathway of the system from low-dimensional stable states with simple structures to high-dimensional complex dynamical behaviors. As σ increases beyond a critical threshold, the emergence of positive LLE values and the proliferation of equilibrium points collectively demonstrate characteristic bifurcation patterns, marking the system's evolution from stability to chaos. To further investigate this transition, we examined the system's response under a different driving frequency ($\omega=10$) while holding the other parameters consistent with the configuration in Fig. 2. The bifurcation diagram is presented in Fig. 3.

The system exhibits a pronounced transition at $\sigma\approx 10$, which is a critical threshold that demarcates the shift from low-dimensional steady states to multistability and chaotic regimes. This transition demonstrates that σ in the memristive function is the principal parameter controlling structural reconfiguration. Our investigations reveal that increasing the external excitation frequency promotes the proliferation of equilibrium points, and facilitates the emergence of chaotic

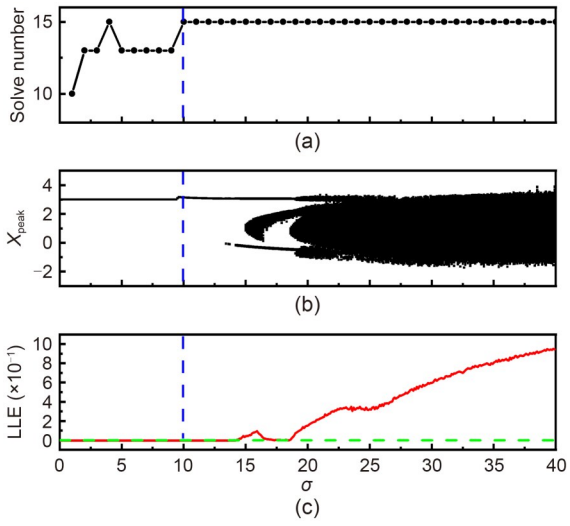

Fig. 2 (a) Number of equilibrium points at $i_s'=5$; (b) peak value in sampled time series for variable x; (c) LLE versus parameter σ. For Figs. 2b and 2c, $i_s'=5\sin(\omega\tau)=5\sin(2.5\tau)$. Parameters are set to: $a=0.1$, $b=7.2$, $c=0.05$, $\delta=1.5$, $\beta'=3.2$, $r=0.1$, $k=0.1$, with initial values (2.00, 2.00, 0.01)

behavior within identical σ parameter ranges. The parameter σ predominantly governs the system's nonlinear activation intensity, while the external excitation frequency modulates the dynamic characteristics and information complexity. Systematic bifurcation analysis is conducted through adjustment of the forcing frequency ω, with the corresponding results presented in Fig. 4.

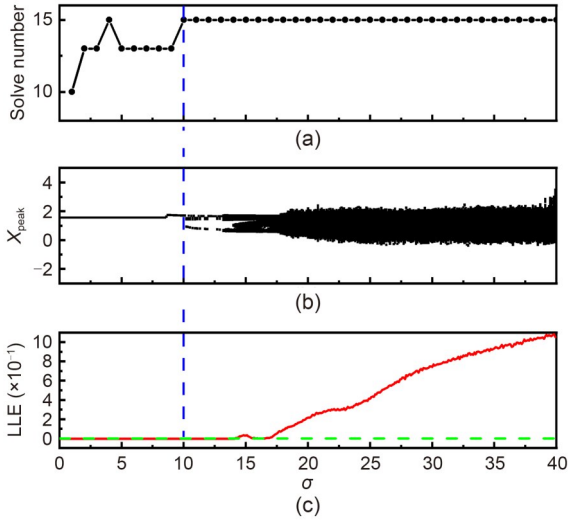

Fig. 3 (a) Number of equilibrium points at i_s'=5; (b) peak value in sampled time series for variable x; (c) LLE versus parameter σ. For Figs. 3b and 3c, i_s'=5sin($\omega\tau$)=5sin(10τ)

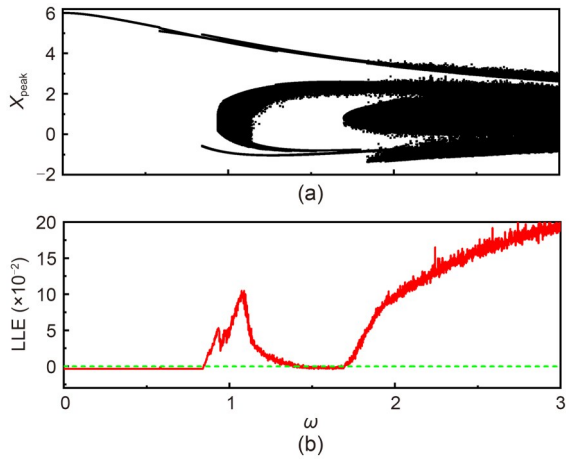

Fig. 4 Distribution of peak values for variable x (a) and LLE versus angular frequency ω (b). The parameters were set to: a=0.1, b=7.2, c=0.05, δ=1.5, σ=20.0, β'=3.2, k=0.1, A=5, and r=0.1

The results demonstrate that the memristive neuron exhibits chaotic patterns when the forcing frequency ω ranges from 0.85 to 1.40 or exceeds 1.7, with higher forcing frequencies being more likely to support chaotic activity. The results in Fig. 4 help identify parameter ranges that can distinguish chaotic and periodic attractors. Furthermore, Fig. 5 illustrates the evolution of attractors and the variable x under varying external stimuli frequencies, providing insights into how firing patterns depend on the excitation frequency.

Under external excitation currents with varying frequencies, the memristive neuron exhibits multiple oscillation modes, including periodic, weakly chaotic, and strongly chaotic states. Specifically, periodic attractors correspond to regular spiking patterns; weakly chaotic attractors maintain overall periodicity while displaying localized chaos in the upper-right region; strongly chaotic attractors display a complete loss of periodicity and have fully irregular dynamics. Analysis of the energy reveals that chaotic neurons maintain lower average energy values <H> compared to periodic neurons, suggesting that energy relationships dominate the mode transitions. Fig. 6 presents a quantitative comparison of energy variations and the proportion of energy components across different regimes.

Fig. 6 demonstrates that the average energy in the strongly chaotic state is markedly lower than in the periodic and weakly chaotic states. The emergence of chaotic behavior shows a direct correlation with the relative proportion of memristive channel energy H_M, where increasing M and L_2 proportions lead to greater chaos in the system. Using the parameter configurations from Figs. 5 and 6, we calculated the voltage variables in the memristive channel to identify the distinct firing patterns, which are displayed in Fig. 7.

When varying the forcing frequency ω to evoke periodic or chaotic electrical activities in neurons, the firing patterns in Fig. 7 exhibit significant frequency-dependent variations, particularly demonstrating strongly chaotic firings. Furthermore, we added Gaussian white noise to the single-variable/branch circuit, and employed both the coefficient variation (C_V) and average energy <H> as quantitative metrics to detect the occurrence of stochastic resonance:

$$\begin{cases} C_V = \dfrac{\sqrt{\langle \Delta_{IS}^2 \rangle - \langle \Delta_{IS} \rangle^2}}{\langle \Delta_{IS} \rangle}, \\ \langle H \rangle = \dfrac{1}{t_1 - t_0} \int_{t_0}^{t_1} H \mathrm{d}\tau = \dfrac{1}{N} \sum_{i=1}^{N} H_i, \end{cases} \tag{16}$$

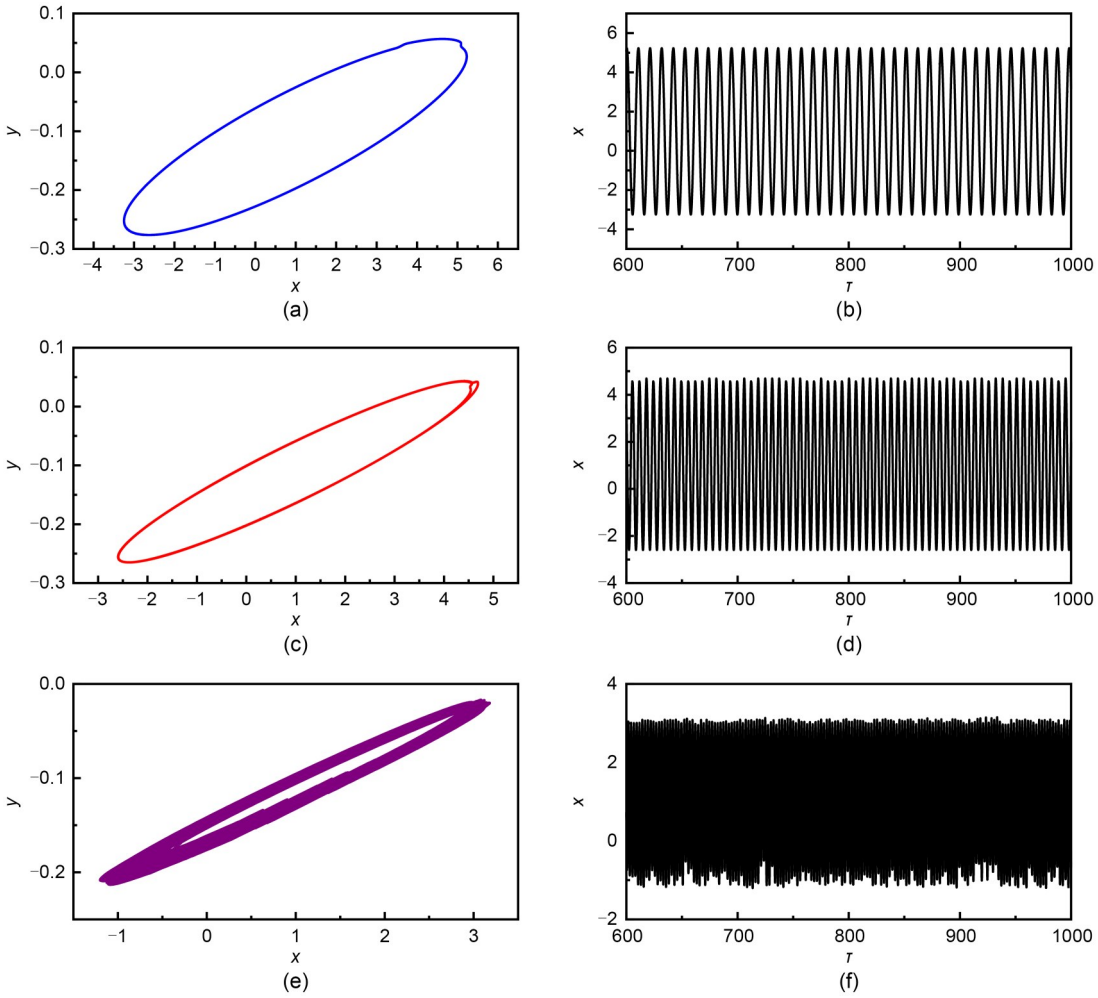

Fig. 5 System attractor (a, c, and e) and evolution of variable x (b, d, and f): (a and b) ω=0.6; (c and d) ω=1.0; (e and f) ω=2.5

where Δ_{IS} is the inter-spike interval, which can be obtained from the sampled variable series for one variable in the model. N describes the maximum count or number of iterations in the numerical calculation. In Fig. 8, the dependence of C_V values and average energy $<H>$ on the noise intensity is estimated to predict the emergence of stochastic resonance; this results in the maximum value for $<H>$ and the lowest value for C_V occurring at a moderate noise intensity.

In Fig. 8, the numerical simulations demonstrate characteristic SR phenomena when the noise intensity reaches appropriate levels, manifesting as highly synchronized neural activity and consistent correspondence between the minimum value for C_V and maximum value for $<H>$. Quantitative analysis reveals that: SR occurs in the L_1 inductive channel (D=0.043) with $<H>$=4.15843 and C_V=0.82792; the L_2 inductive channel (D=0.076) exhibits an enhanced SR response ($<H>$=4.19763 and C_V=0.81505); the memristive channel shows SR at D=0.058 ($<H>$=4.17200 and C_V=0.81990). A comparative analysis indicates that the L_2 channel achieves optimal SR performance under noise excitation, demonstrating both the highest $<H>$ value and the lowest C_V value, which suggests its superior responsiveness to noise modulation. Furthermore, Fig. 9 presents a comparison of the response characteristics of the neuron when three branch circuits are simultaneously excited by identical noise excitations.

It is worth noting that when the three variables in Eq. (6) are simultaneously excited by the same noise, the system also exhibits SR at moderate noise intensity. In the unique configuration of a purely magnetic circuit, the energy exchange among the three

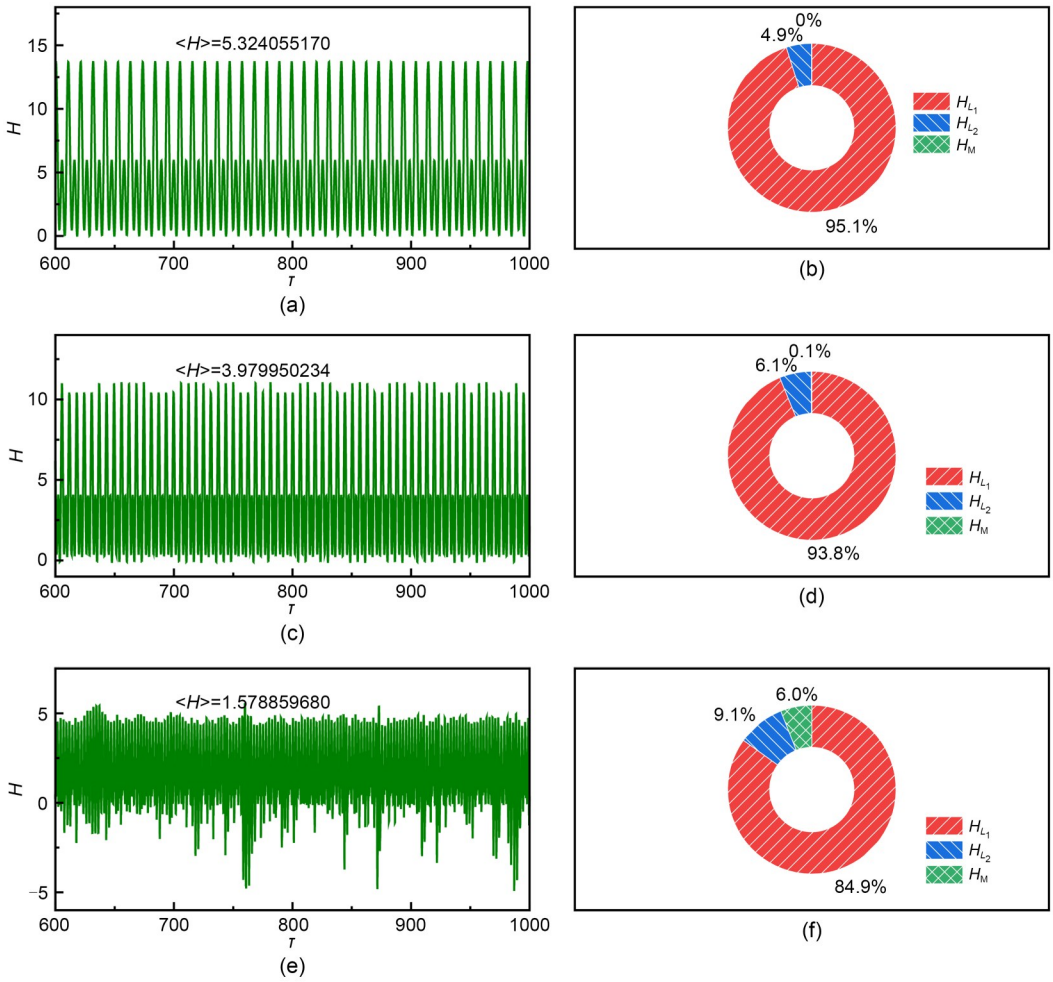

Fig. 6 Evolution of the energy function (a, c, and e) and energy proportion for each energy term in the neuron presenting with different firing patterns (b, d, and f): (a and b) ω=0.6; (c and d) ω=1.0; (e and f) ω=2.5

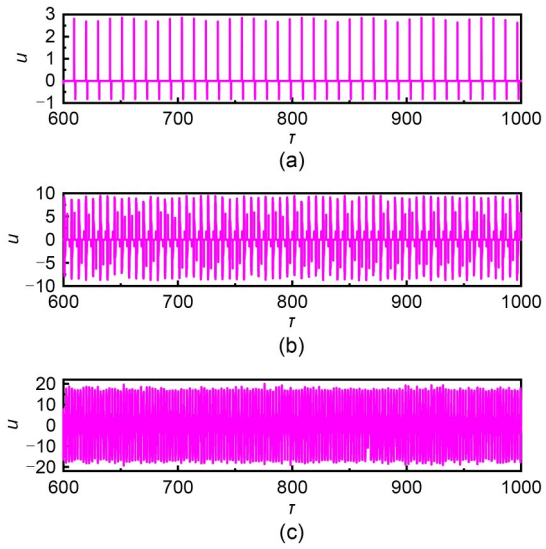

Fig. 7 Evolution of the memristive variable u in Eq. (6): (a) ω=0.6; (b) ω=1.0; (c) ω=2.5

channels/branches becomes much more intricate. Compared to the single-channel stimulation case illustrated in Fig. 8, the enhanced inter-channel coupling notably raises the noise intensity threshold required to achieve SR. Moreover, under multi-channel excitation, the maximum value of <H> exceeds the value that was observed under single-channel noise, while the C_V value falls below the minimum C_V recorded in the single-channel scenario. These findings indicate that synergistic interactions among multiple channels contribute to a more effective activation of SR, highlighting the advantages of multi-branch magnetic structures in enhancing neural circuit functionality. To further investigate adaptive regulation based on the mode selection in neural activities, an adaptive control scheme for the parameter σ following the energy regulation is suggested as follows:

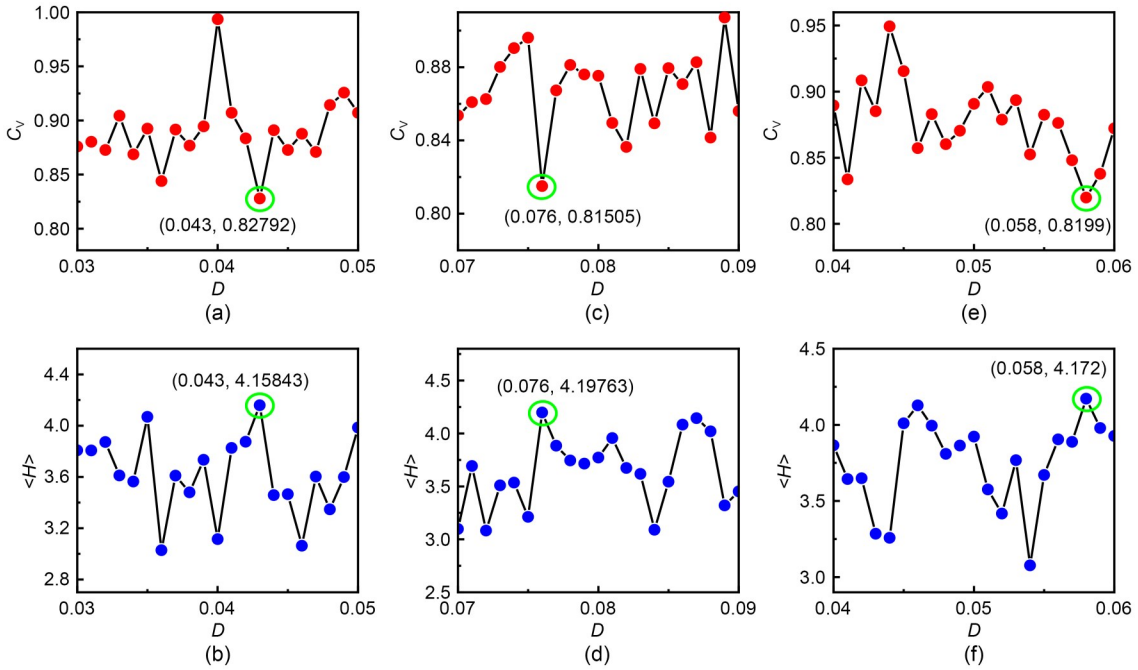

Fig. 8 Distribution of C_V (a, c, and e) and <H> (b, d, and f) values versus noise intensity D at ω=1.0: (a and b) noise excitation on variable x; (c and d) noise excitation on variable y; (e and f) noise excitation on variable z

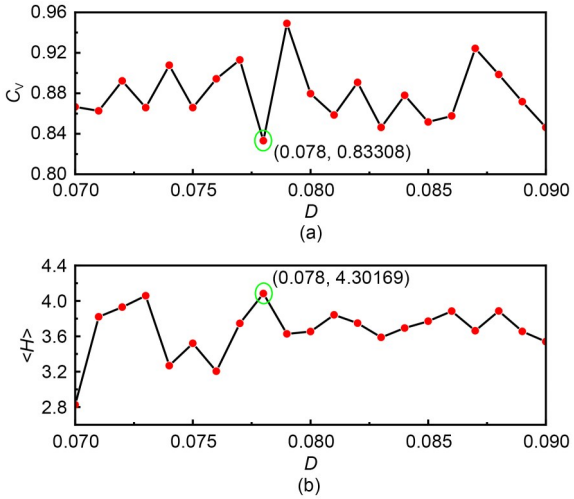

Fig. 9 Distribution of C_V and <H> values versus noise intensity D at ω=1.0

$$\frac{\mathrm{d}\sigma}{\mathrm{d}\tau}=-g\sigma\cdot\theta\left(\left|\frac{H_{\mathrm{M}}(\tau)}{H(\tau)}\right|-\varepsilon\right),\quad \tau>650,\ \theta(v)=\begin{cases}1, & v\geqslant 0,\\ 0, & v<0.\end{cases} \tag{17}$$

In this control scheme, the proportional threshold ε determines the ratio of memristive channel energy to the total electric field energy of the neuron, the parameter g controls the growth rate of the gain σ for memristive current, and θ represents the Heaviside function. Adaptive control is activated at τ>650 so that the neuron is activated during the transition period, showing a stable firing pattern.

As shown in Fig. 10a, when the parameter g=0.03, the control parameter σ stabilizes at 11.33769 after 872.62 (=650+222.62) time units. Under adaptive control, the neural activities show distinct transitions from chaotic to periodic states, which are accompanied by significant changes in the energy function. The results in Fig. 10 confirm that increasing the parameter g will significantly reduce the time before the parameter σ attains a saturation value, thereby accelerating the transition from chaotic to periodic states. The memristive variable u of the memristor also changes to a periodic oscillation.

In summary, activation of energy flow across the magnetic field is effective for supporting continuous changes in the neural circuit composed of inductive components and MFCM. Moreover, this memristive neuron without a capacitive variable still presents similar firing patterns as known neuron models. Our proposed neuron generates diverse firing patterns, which can be characterized by measuring the voltage across the MFCM in the neural circuit. Its oscillatory mechanism results from continuous energy exchange between the memristive channel and inductive channels.

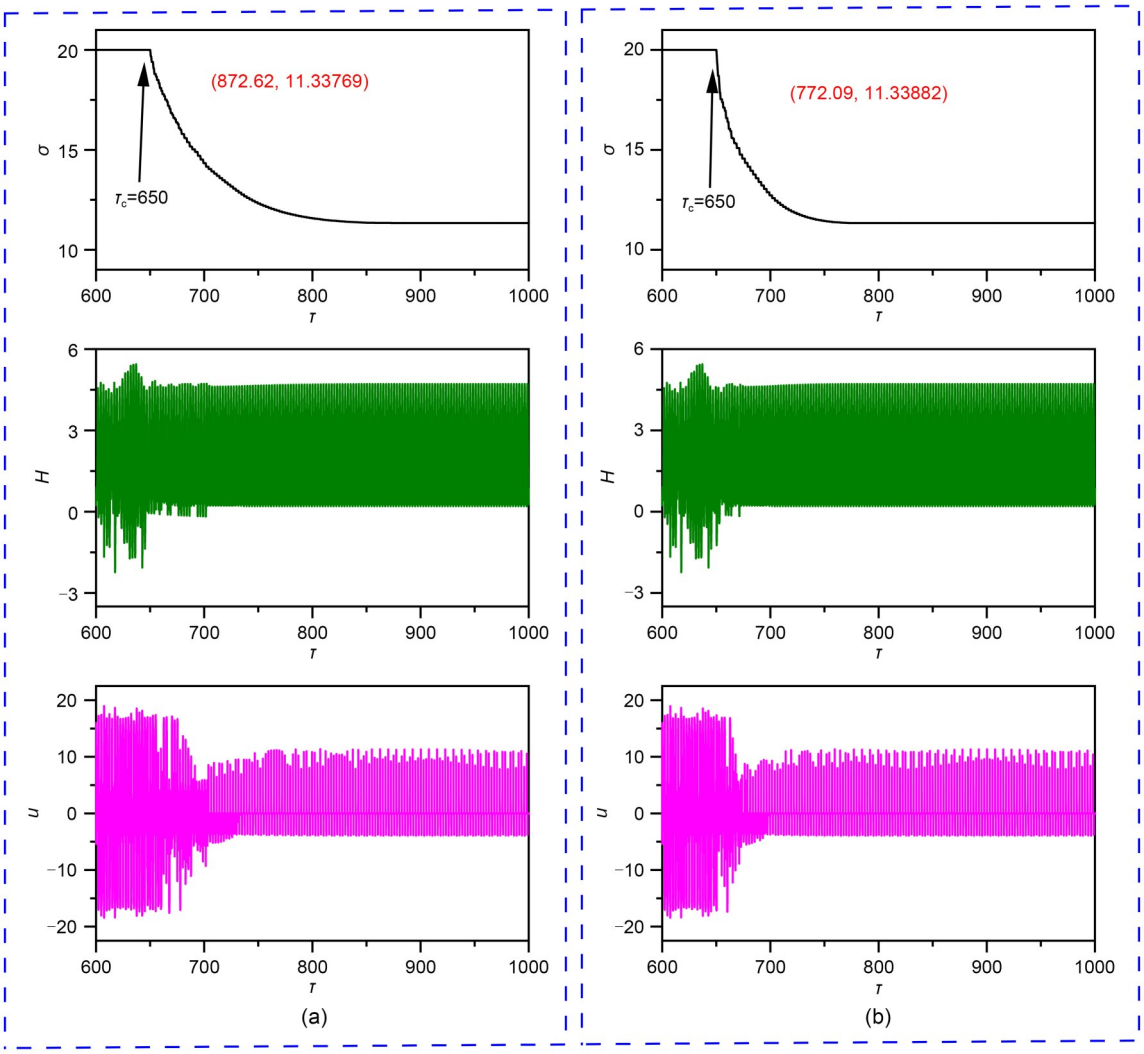

Fig. 10 Change of parameter σ in Eq. (6) with the evolution of Hamilton energy H and memristive variable u: (a) g=0.03; (b) g=0.05. The parameters are set to: a=0.1, b=7.2, c=0.05, β'=3.2, k=0.1, A=5.0, ω=2.5, r=0.1, and ε=0.3

The numerical results confirm that continuous energy exchange serves as the physical foundation for sustaining neuronal oscillations and stable firing patterns. Notably, the high-order nonlinearity of the memristor governs the emergence of chaotic behavior by determining the number of equilibrium points. Precise adjustment of the external stimulation frequency ω enables controlled transitions between firing patterns and effective energy level modulation, while significant SR is induced under appropriate noise intensity. This novel pure magnetic-field circuit architecture may aid both neurodynamic research and neuromorphic device design. In recent decades, memristors with varying memristive functions have been used to design and control nonlinear circuits. The initial dependence and memory properties enable multi-stability and applications in neural circuits; as such, functional neurons with clear physical descriptions have been developed (Ascoli and Corinto, 2013; Babacan et al., 2016; Wu and Wang, 2023; Shao et al., 2024; Shi et al., 2024). In particular, this approach offers an exact energy definition for the memristive oscillator, and the memristive map provides physical explanations for the memristive systems (Du et al., 2022; Li and Chen, 2023; Mao et al., 2025; Shi et al., 2025). Moreover, the energy balance supports synchronization and regularized patterns in coupled biophysical models. In addition, with reliable neuron models, energy control can be helpful for preventing nervous disorders (Hou et al., 2024; Zhao et al., 2024). At the same time,

the proposed neuron models can be further updated with equivalent map neurons (Guo et al., 2024; Jia JE et al., 2024) by applying linear transformations or the Euler difference algorithm. Additionally, digital implementation of neuron models via a field-programmable gate array (FPGA) (Graas et al., 2004; Wang and Luo, 2022; Liu et al., 2024) enables rapid parallel computing of neural signals in coupled circuit arrays, which can be used to improve control of electromechanical devices through maintenance of neural signals.

4 Open problems

Memristive terms for CCM and MFCM are presented in high-order nonlinear forms; the linear parts account for the consumption of Joule heat, while the nonlinear terms are associated with the field energy effect. To keep dimensional homogeneity and remove the effect of physical parameters in the theoretical models, double intrinsic parameters should be introduced into the memristive function for the memristor as follows:

$$\begin{cases} i_{\mathrm{M}}=M(\phi)V_{\mathrm{M}}=\delta_1\csc(\delta_2\phi)V_{\mathrm{M}}, \\ \quad \text{or, } \delta_1\tanh(\delta_2\phi)V_{\mathrm{M}}, \text{ for MFCM}, \\ V_{\mathrm{M}}=W(q)i_{\mathrm{M}}=\delta_3\csc(\delta_4 q)i_{\mathrm{M}}, \\ \quad \text{or, } \delta_3\tanh(\delta_4 q)i_{\mathrm{M}}, \text{ for CCM}, \end{cases} \tag{18}$$

where q represents the electric charge. In this way, the gains in the nonlinear terms csc(*) and tanh(*) of the theoretical models become dimensionless; otherwise, they still have new physical units. For the first formula in Eq. (1), the coefficient δ_2 for the kernel variable (magnetic flux) is endowed with 1; without clarifying this assumption, the new parameter σ ($=L_1E_1/R_2$) will maintain the physical unit. Following the generic definition in the first formula in Eq. (18), the coefficient δ_2 can be combined as dimensionless gain $\sigma=L_1E_1\delta_2/R_2$, and then the scale transformation becomes perfect for supporting a dimensionless theoretical model in Eq. (6). For forthcoming studies, researchers should introduce suitable parameter (δ_2 or δ_4) for the kernel variable, and the developed theoretical model derived from circuit equations after scale transformation becomes dimensionless completely, in which all variables and parameters have no physical units.

5 Conclusions

An MFCM was incorporated into a branch circuit of a capacitor-free linear circuit, transforming the circuit into a pure magnetic-field system; this memristive term/channel played an important role in shunting energy and regulating nonlinear energy without using any capacitive variables. Conventional theory holds that oscillatory circuits and their equivalent nonlinear oscillators arise from energy exchange between storage elements for electric fields and magnetic fields, and that pure magnetic-field circuits are generally incapable of such energy interactions. However, in this study, we successfully demonstrated energy exchange in a pure magnetic-field circuit through a novel MFCM-based neural circuit, and it was confirmed that the energy proportion in the magnetic channel significantly influences the system's firing modes. Moreover, simulation results showed that under different external stimulation frequencies, the MFCM acts as a temporary energy storage unit, inducing various firing patterns by activating electromagnetic induction in the memristive channel.

Our proposed scheme demonstrates that the combination of an inductor and an MFCM can establish a functional neural circuit that does not require capacitors. In the developed memristive model, the energy function exhibits unique determinacy. The capacitor-free design not only eliminates geometric constraints associated with capacitors, but also enables the memristor terminal voltage to be directly equated to neuron membrane potential. The findings further showcase that efficient neural circuit implementation can be achieved through the proper configuration of non-capacitive electrical elements, such as inductors, resistors, and MFCMs. This work advances beyond the conventional limitation that pure magnetic-field circuits cannot achieve continuous energy exchange, and provides a theoretical foundation for developing novel capacitor-free neural circuits where even nonlinear resistors may not be used. This novel incorporation of an MFCM expands memristor applications in nonlinear circuits, and potentially opens technical pathways for biomimetic neuromorphic computing systems in the future. Subsequent research will focus on optimizing the dynamic characteristics of incorporated MFCMs, as well as the performance and adaptability of memristive models in computational neuroscience.

Acknowledgments

This work is supported by the National Natural Science Foundation of China (No. 62361037).

Author contributions

Jun MA and Zhao LEI designed the research. Zhao LEI and Qun GUO processed the corresponding data. Zhao LEI wrote the first draft of the manuscript. Chunni WANG supported funding for this research. Jun MA and Chunni WANG revised and edited the final version.

Conflict of interest

Zhao LEI, Qun GUO, Chunni WANG, and Jun MA declare that they have no conflict of interest.

References

Altan MA, Orman K, Babacan Y, et al., 2024. Special memristor and memristor-based compact neuron circuit. *Journal of Circuits, Systems and Computers*, 33(5):2450091. https://doi.org/10.1142/S0218126624500919

Ascoli A, Corinto F, 2013. Memristor models in a chaotic neural circuit. *International Journal of Bifurcation and Chaos*, 23(3):1350052. https://doi.org/10.1142/S0218127413500521

Babacan Y, Kaçar F, Gürkan K, 2016. A spiking and bursting neuron circuit based on memristor. *Neurocomputing*, 203: 86-91. https://doi.org/10.1016/j.neucom.2016.03.060

Brütt M, Kaernbach C, 2021. On the role of the excitation/inhibition balance of homeostatic artificial neural networks. *Entropy*, 23(12):1681. https://doi.org/10.3390/e23121681

Buzsáki G, Draguhn A, 2004. Neuronal oscillations in cortical networks. *Science*, 304(5679):1926-1929. https://doi.org/10.1126/science.1099745

Chen L, Li XL, Tjia M, et al., 2022. Homeostatic plasticity and excitation-inhibition balance: the good, the bad, and the ugly. *Current Opinion in Neurobiology*, 75:102553. https://doi.org/10.1016/j.conb.2022.102553

Chen ZQ, Tang H, Wang ZL, et al., 2015. Design and circuit implementation for a novel charge-controlled chaotic memristor system. *Journal of Applied Analysis & Computation*, 5(2):251-261. https://doi.org/10.11948/2015023

Cheng S, Wang NG, Arnold DP, 2007. Modeling of magnetic vibrational energy. harvesters using equivalent circuit representations. *Journal of Micromechanics and Microengineering*, 17(11):2328. https://doi.org/10.1088/0960-1317/17/11/021

Chua L, 1971. Memristor–the missing circuit element. *IEEE Transactions on Circuit Theory*, 18(5):507-519. https://doi.org/10.1109/TCT.1971.1083337

Dagar S, Chowdhury SR, Bapi RS, et al., 2016. Near-infrared spectroscopy-electroencephalography-based brain-state-dependent electrotherapy: a computational approach based on excitation-inhibition balance hypothesis. *Frontiers in Neurology*, 7:123. https://doi.org/10.3389/fneur.2016.00123

Douglas RJ, Martin KAC, 2004. Neuronal circuits of the neocortex. *Annual Review of Neuroscience*, 27:419-451. https://doi.org/10.1146/annurev.neuro.27.070203.144152

Du SC, Deng Q, Hong QH, et al., 2022. A memristor-based circuit design and implementation for blocking on Pavlov associative memory. *Neural Computing and Applications*, 34(17):14745-14761. https://doi.org/10.1007/s00521-022-07162-z

Froemke RC, Merzenich MM, Schreiner CE, 2007. A synaptic memory trace for cortical receptive field plasticity. *Nature*, 450(7168):425-429. https://doi.org/10.1038/nature06289

Gao R, Peterson EJ, Voytek B, 2017. Inferring synaptic excitation/inhibition balance from field potentials. *NeuroImage*, 158:70-78. https://doi.org/10.1016/j.neuroimage.2017.06.078

Graas EL, Brown EA, Lee RH, 2004. An FPGA-based approach to high-speed simulation of conductance-based neuron models. *Neuroinformatics*, 2(4):417-435. https://doi.org/10.1385/NI:2:4:417

Guo YT, Ma J, 2025. An electromechanical arm model controlled by artificial muscles. *Science China Technological Sciences*, 68(4):1420403. https://doi.org/10.1007/s11431-024-2855-3

Guo YT, Ma J, Zhang XF, et al., 2024. Memristive oscillator to memristive map, energy characteristic. *Science China Technological Sciences*, 67(5):1567-1578. https://doi.org/10.1007/s11431-023-2637-1

Hou S, Wang HD, Fan DG, et al., 2024. The effects of negative regulation on the dynamical transition in epileptic network. *International Journal of Bifurcation and Chaos*, 34(3):2450038. https://doi.org/10.1142/S021812742450038X

Indiveri G, Linares-Barranco B, Hamilton TJ, et al., 2011. Neuromorphic silicon neuron circuits. *Frontiers in Neuroscience*, 5:73. https://doi.org/10.3389/fnins.2011.00073

Isaac JTR, Crair MC, Nicoll RA, et al., 1997. Silent synapses during development of thalamocortical inputs. *Neuron*, 18(2):269-280. https://doi.org/10.1016/s0896-6273(00)80267-6

Izhikevich EM, 2006. Dynamical Systems in Neuroscience: the Geometry of Excitability and Bursting. MIT Press, Cambridge, Massachusetts, USA. https://doi.org/10.7551/mitpress/2526.001.0001

Jia JE, Wang CN, Zhang XF, et al., 2024. Energy and self-adaption in a memristive map neuron. *Chaos, Solitons & Fractals*, 182:114738. https://doi.org/10.1016/j.chaos.2024.114738

Jia JN, Yang FF, Ma J, 2023. A bimembrane neuron for computational neuroscience. *Chaos, Solitons & Fractals*, 173: 113689. https://doi.org/10.1016/j.chaos.2023.113689

Jia JN, Xie Y, Wang CN, et al., 2024. Thermosensitive double-membrane neurons and their network dynamics. *Physica Scripta*, 99(11):115030. https://doi.org/10.1088/1402-4896/ad86f6

Katz LC, Shatz CJ, 1996. Synaptic activity and the construction of cortical circuits. *Science*, 274(5290):1133-1138. https://doi.org/10.1126/science.274.5290.1133

Kirischuk S, 2022. Keeping excitation–inhibition ratio in balance. *International Journal of Molecular Sciences*, 23(10): 5746. https://doi.org/10.3390/ijms23105746

Lei Z, Ma J, 2025. Coherence resonance and energy dynamics in a memristive map neuron. *Chaos: An Interdisciplinary Journal of Nonlinear Science*, 35(2):023158. https://doi.org/10.1063/5.0251352

Li CL, Yang YY, Du JR, et al., 2021. A simple chaotic circuit with magnetic flux-controlled memristor. *The European Physical Journal Special Topics*, 230(7):1723-1736. https://doi.org/10.1140/epjs/s11734-021-00181-2

Li SQ, Liu Z, Zhao H, et al., 2016. Wireless power transfer by electric field resonance and its application in dynamic charging. *IEEE Transactions on Industrial Electronics*, 63(10):6602-6612. https://doi.org/10.1088/0960-1317/17/11/021

Li ZJ, Chen KJ, 2023. Neuromorphic behaviors in a neuron circuit based on current-controlled Chua corsage memristor. *Chaos, Solitons & Fractals*, 175:114017. https://doi.org/10.1016/j.chaos.2023.114017

Liu F, Li HY, Hu W, et al., 2024. Review of neural network model acceleration techniques based on FPGA platforms. *Neurocomputing*, 610:128511. https://doi.org/10.1016/j.neucom.2024.128511

Ma J, 2023. Biophysical neurons, energy, and synapse controllability: a review. *Journal of Zhejiang University-SCIENCE A (Applied Physics & Engineering)*, 24(2): 109-129. https://doi.org/10.1631/jzus.A2200469

Ma J, Yang ZQ, Yang LJ, et al., 2019. A physical view of computational neurodynamics. *Journal of Zhejiang University-SCIENCE A (Applied Physics & Engineering)*, 20(9):639-659. https://doi.org/10.1631/jzus.A1900273

Mao YD, Dong YJ, Lu ZZ, et al., 2025. Second-order locally active memristor based neuronal circuit. *Chaos, Solitons & Fractals*, 195:116279. https://doi.org/10.1016/j.chaos.2025.116279

Moon J, Leeb SB, 2016. Power electronic circuits for magnetic energy harvesters. *IEEE Transactions on Power Electronics*, 31(1):270-279. https://doi.org/10.1109/TPEL.2015.2401336

Pershin YV, di Ventra M, 2011. Memory effects in complex materials and nanoscale systems. *Advances in Physics*, 60(2):145-227. https://doi.org/10.1080/00018732.2010.544961

Schroedermeier A, Ludois DC, 2017. Integrated inductor and capacitor with co-located electric and magnetic fields. *IEEE Transactions on Industry Applications*, 53(1):380-390. https://doi.org/10.1109/TIA.2016.2604219

Shao Y, Wu FQ, Wang QY, 2024. Synchronization and complex dynamics in locally active threshold memristive neurons with chemical synapses. *Nonlinear Dynamics*, 112(15):13483-13502. https://doi.org/10.1007/s11071-024-09747-w

Shi F, Cao YH, Banerjee S, et al., 2025. A neuronal circuit based on a second-order memristor. *Nonlinear Dynamics*, 113(10):12165-12183. https://doi.org/10.1007/s11071-024-10662-3

Shi SY, Liang Y, Li YQ, et al., 2024. A neuron circuit based on memristor and negative capacitor: dynamics analysis and hardware implementation. *Chaos, Solitons & Fractals*, 180:114534. https://doi.org/10.1016/j.chaos.2024.114534

Sporns O, 2010. Networks of the Brain. MIT Press, Cambridge, Massachusetts, USA. https://doi.org/10.7551/mitpress/8476.001.0001.

Strukov DB, Snider GS, Stewart DR, et al., 2008. The missing memristor found. *Nature*, 453(7191):80-83. https://doi.org/10.1038/nature06932

Takembo CN, Mvogo A, Ekobena Fouda HP, et al., 2019. Effect of electromagnetic radiation on the dynamics of spatiotemporal patterns in memristor-based neuronal network. *Nonlinear Dynamics*, 95(2):1067-1078. https://doi.org/10.1007/s11071-018-4616-0

Wan JY, Wu FQ, Ma J, et al., 2024. Dynamics and synchronization of neural models with memristive membranes under energy coupling. *Chinese Physics B*, 33(5):050504. https://doi.org/10.1088/1674-1056/ad1dcc

Wang BC, Lv M, Zhang XF, et al., 2024. Dynamics in a light-sensitive neuron with two capacitive variables. *Physica Scripta*, 99(5):055225. https://doi.org/10.1088/1402-4896/ad37b1

Wang CH, Luo ZQ, 2022. A review of the optimal design of neural networks based on FPGA. *Applied Sciences*, 12(21): 10771. https://doi.org/10.3390/app122110771

Wang CN, Tang J, Ma J, 2019. Minireview on signal exchange between nonlinear circuits and neurons via field coupling. *The European Physical Journal Special Topics*, 228(10):1907-1924. https://doi.org/10.1140/epjst/e2019-800193-8

Wang XJ, 2010. Neurophysiological and computational principles of cortical rhythms in cognition. *Physiological Reviews*, 90(3):1195-1268. https://doi.org/10.1152/physrev.00035.2008

Wu FQ, Wang RB, 2023. Synchronization in memristive HR neurons with hidden coexisting firing and lower energy under electrical and magnetic coupling. *Communications in Nonlinear Science and Numerical Simulation*, 126: 107459. https://doi.org/10.1016/j.cnsns.2023.107459

Xu Q, Fang YJ, Feng CT, et al., 2024a. Firing activity in an

N-type locally active memristor-based Hodgkin-Huxley circuit. *Nonlinear Dynamics*, 112(15):13451-13464. https://doi.org/10.1007/s11071-024-09728-z

Xu Q, Ding XC, Wang N, et al., 2024b. Spiking activity in a memcapacitive and memristive emulator-based bionic circuit. *Chaos, Solitons & Fractals*, 187:115339. https://doi.org/10.1016/j.chaos.2024.115339

Yang FF, Ma J, Ren GD, 2024a. A Josephson junction-coupled neuron with double capacitive membranes. *Journal of Theoretical Biology*, 578:111686. https://doi.org/10.1016/j.jtbi.2023.111686

Yang FF, Ma J, Wu FQ, 2024b. Review on memristor application in neural circuit and network. *Chaos, Solitons & Fractals*, 187:115361. https://doi.org/10.1016/j.chaos.2024.115361

Zhao JY, Yu Y, Han F, et al., 2024. Dynamic modeling and closed-loop modulation for absence seizures caused by abnormal glutamate uptake from astrocytes. *Nonlinear Dynamics*, 112(5):3903-3916. https://doi.org/10.1007/s11071-023-09218-8